Synthesis of yolk/shell Fe₃O₄–polydopamine–graphene–Pt nanocomposite with high electrocatalytic activity for fuel cells

Yingqiang Huang [a], Yingju Liu [a,b,*], Zhuohong Yang [a], Jinliang Jia [a], Xin Li [a], Yan Luo [a], Yueping Fang [a]

[a] Institute of Biomaterials, Department of Applied Chemistry, College of Sciences, South China Agricultural University, Guangzhou 510642, China
[b] State Key Laboratory of Chem/Biosensing & Chemometrics, Hunan University, Changsha 410082, China

HIGHLIGHTS

- A novel yolk/shell Fe₃O₄–polydopamine–graphene–Pt nanocomposite was synthesized.
- The detailed formation mechanism was discussed.
- The yolk/shell nanocomposite showed a high electrocatalytic activity for methanol oxidation.

ARTICLE INFO

ABSTRACT

A novel yolk/shell Fe₃O₄–polydopamine–graphene–Pt (Fe₃O₄@PDA/RGO/Pt) nanocomposite is synthesized using polydopamine as a moderate modifier for graphene as well as a coupling agent for the assembly of Pt nanoparticles. The morphology and structure of the as-prepared catalysts are characterized by transmission electron microscopy, X-ray photoelectron spectroscopy, X-ray diffraction and Fourier transform infrared spectroscopy. The detailed formation mechanism of such yolk/shell nanocomposite is discussed. Subsequently, its catalytic activity towards the methanol oxidation is evaluated by cyclic voltammetry, chronoamperometry, electrochemical impedance spectra and CO-stripping voltammetry. Results show that such york/shell Fe₃O₄@PDA/RGO/Pt exhibits higher electrochemical activity and stability to methanol oxidation than Pt/graphene, which is not only attributed to the synergetic cocatalytic effect at the heterojunction interfaces between the Pt nanoparticles and the support, but also due to the high immobilization of Pt nanoparticles by the functional groups of polydopamine. In addition, the separation ability of Pt nanoparticles from the nanocomposite by Fe₃O₄ can decrease the CO poison from free Pt nanoparticles. Therefore, this unique yolk/shell nanocomposite may be suitable for the production of catalysts with low-cost and high activity.

1. Introduction

Direct methanol fuel cells (DMFCs) have been considered as a promising power source for portable electronic devices and electric vehicles due to the increase in environmental pollution and the depletion of fossil fuels [1]. However, the performance of DMFCs is greatly hampered by the poisoning of the Pt surface by CO-like species during methanol oxidation. In addition, the high cost of

noble metal is also the major challenge [2]. Therefore, many efforts have been developed to overcome these limitations.

It is well known that some Pt-based alloys or Pt-metal oxide catalysts exhibit a higher CO tolerance ability, based on a bifunctional mechanism [3] or an electronic effect [4]. Especially, transition metal oxides are shown to effectively promote methanol electrooxidation, such as Pt/CeO₂–C [5] and Pt–ZrO₂/CNT [6]. It is proposed that the oxygen-containing species could be more easily formed on the surface of metal oxides, which can favor the oxidation of CO or CHO on the neighboring poisoned Pt sites and release the Pt active sites for further methanol oxidation [7]. However, during the preparation of metal-oxide based Pt catalysts, Pt can not only deposit around the metal-oxides, but also exist alone in the reaction mixture, which can still influence methanol electrooxidation. Therefore, it is important to separate these free Pt

nanoparticles from the metal-oxide loaded Pt catalysts. Recently, magnetic Fe_3O_4 nanoparticles have already shown preeminent applications in magnetic fluids, magnetic resonance imaging, environmental remediation and data storage, due to its magnetic properties and cheapness [8]. Thus, it is possible to use magnetic Fe_3O_4 nanocomposites as the metal oxide of the catalyst, and also as an effective separation substance of free Pt nanoparticles from catalysts.

In addition, the support of the catalysts is very important since it can influence the activity and durability of the catalysts. Various carbon materials have been investigated as catalyst supports in DMFCs including carbon nanotubes [2,6], carbon nanofibers [9], carbon nanorods [10], carbon nanospheres [11] and graphene [1]. Graphene, a single layer of carbon atoms in a hexagonal lattice, has recently attracted much attention due to its unique chemical and physical properties, such as high surface area, high conductivity and chemical stability [1,12]. During the reduction of graphene oxide (GO) to the reduced graphene oxide (RGO), the common dangerous reagents are hydrazine, dimethylhydrazine or $NaBH_4$ [13,14]. Additionally, RGO sheets tend to form agglomerates because of their decreased hydrophilicity, or even re-stack into graphite because of the absence surface modification with surfactants or block polymers [15]. Up to now, several approaches, such as chemical vapor deposition or thermal annealing GO with NH_3, have been employed to reduce GO by occupying the interface of molecules and nanoscale objects in GO sheets; however, rigorous conditions or special instruments are required [16,17]. Therefore, many mild and effective means have been explored for GO reduction, while pursuing the excellent stability and dispersity of RGO in water. Recently, Chen and co-workers synthesized nitrogen-doped graphene hydrogel by ethylenediamine and reduced GO by a simple hydrothermal method [18]. Dopamine, as a unique molecule mimicking protein, can be self-polymerized to form polydopamine (PDA) in weak alkaline solution, which can modify almost all material surfaces including noble metals, metal oxides, semiconductors, ceramics and synthetic polymers [14]. Due to its high amounts of catechol and amino groups, PDA can be served as a versatile platform to immobilize more metal nanoparticles, and also employed to react with GO through a mild hydrothermal process.

It is well known that the catalytic activity is strongly dependent on the shape, size, and size distribution of catalytic particles. The yolk/shell nanoparticles represent a new type of special core/shell structures with a distinctive core/void/shell configuration. Due to the specific surface area and low density, they have been found various applications in fuel cells [19]. For example, Geng and co-workers found that Au–Pt yolk/shell nanostructure exhibited a superior Pt-based electrocatalytic activity for DMFC with notable CO-tolerance [20]. Yang and co-workers synthesized noble metal nanoparticles with hollow or cage-bell structures, which displayed excellent methanol tolerance for oxygen reduction reaction at the cathode of the DMFC [19]. Qiao and co-workers found that Pd nanoparticles in the hybrid PMO yolk/shell structures catalysts exhibited a high conversion and selectivity in alcohol oxidation [21].

In this work, Fe_3O_4 nanoparticles were prepared by a simple hydrothermal method, and then spherical Fe_3O_4@PDA particles with well-defined core/shell nanostructures were synthesized by the self-polymerization of dopamine. Subsequently, Fe_3O_4@PDA/RGO was synthesized by using Fe_3O_4@PDA and GO as the precursors through a mild hydrothermal process, and Pt nanoparticles were finally deposited on the Fe_3O_4@PDA/RGO surface by ethylene glycol reduction. Such yolk/shell nanocomposite was characterized by transmission electron microscopy (TEM), X-ray photoelectron spectroscopy (XPS), X-ray diffraction (XRD) and Fourier transform infrared spectroscopy (FT-IR). The detailed formation mechanism of Fe_3O_4@PDA/RGO/Pt catalyst was discussed. Finally, the electrocatalytic properties of the as-prepared Fe_3O_4@PDA/RGO/Pt catalyst for methanol electrooxidation were investigated by cyclic voltammetry (CV), chronoamperometry, electrochemical impedance spectra (EIS) and CO-stripping voltammetry.

2. Experimental

2.1. Chemicals and materials

All chemicals were of analytical grade and used as received without further purification. Ferric chloride hexahydrate, anhydrous sodium acetate, 1,6-diaminohexane and ethylene glycol were purchased from Sinopharm Chemical Reagent Co., Ltd. Natural graphite flake (325 mesh) was supplied by Alfa Aesar. $H_2PtCl_6 \cdot 6H_2O$ (99.7%) was purchased from Jiuyue Company, Shanghai. Dopamine hydrochloride was obtained from Aladdin and Nafion solution (5%) was purchased from Dupont Company, respectively.

2.2. Synthesis of graphene oxide and amine-functionalized magnetic nanoparticles

Graphene oxide was synthesized from natural graphite flakes by a modified Hummers method [12]. In a typical procedure, the amine-functionalized magnetic Fe_3O_4 nanoparticles were prepared through a solvothermal reaction [22]. Briefly, $FeCl_3 \cdot 6H_2O$ (0.9 g), 1,6-diaminohexane (7.5 g) and anhydrous sodium acetate (2.0 g) were dissolved in ethylene glycol (30 mL) with magnetic stirring at 50 °C to obtain a transparent solution. Then, the solution was transferred to a Teflon-lined stainless-steel autoclave and heated at 205 °C. After 6 h, the autoclave was automatically cooled to room temperature. The magnetic nanoparticles were washed with water and ethanol for 3 times, and then dried at 50 °C for 6 h.

2.3. Synthesis of Fe_3O_4@PDA/RGO/Pt nanocomposites

To synthesize Fe_3O_4@PDA composites, 50 mg of the as-prepared Fe_3O_4 was dispersed in 250 mL of water under ultrasonication. After 30 min, 75.0 mg of dopamine hydrochloride was added and sonicated for 30 min. Then, 302.9 mg of Tris was added and stirred for 8 h. The resultant was separated and collected with a magnet, washed and redispersed in 40 mL of distilled water.

To synthesize Fe_3O_4@PDA/RGO composites, 40 mg of GO was dispersed in 40 mL of water under ultrasonication for 30 min, and mixed with 40 mL of Fe_3O_4@PDA solution. After sonication for 20 min, the mixture was transferred into an autoclave and heated at 130 °C for 8 h. The product was separated by the magnet, washed and dried at 50 °C for 6 h.

In a typical synthesis of Fe_3O_4@PDA/RGO/Pt composite, Fe_3O_4@PDA/RGO was dispersed in ethylene glycol/water mixture (40 mL, 40 V% ethylene glycol content) by ultrasonication for 10 min, and a certain volume of 0.0772 M H_2PtCl_6 were added and stirred for 2 h. Then, the solution was refluxed for 2 h, where the color changed from nearly colorless to black. After that, the precipitate was magnetically separated and washed to remove free Pt particles. Finally, the catalysts were dried at 50 °C. By changing the mass contents of Pt in the catalyst, different catalysts were synthesized. The catalysts with 9, 12, and 15 wt.% of Pt content were denoted as Fe_3O_4@PDA/RGO/Pt (9%), Fe_3O_4@PDA/RGO/Pt (12%) and Fe_3O_4@PDA/RGO/Pt (15%), respectively. For comparison, Pt/graphene (15 wt.% Pt content) sample was also prepared using a similar procedure as above.

2.4. Structure and morphology characterization

The structure and morphology of the catalysts were analyzed using TEM (Netherlands, FEI Tecnai 12 operated at 100 kV) and FT-IR spectra were recorded from 4000 to 400 cm^{-1} on a Spectrometer (VERTEX 70, Bruker, German) at the Instrumental Analysis & Research Center in South China Agriculture University. Powder X-ray diffraction (XRD) patterns were collected on a Bruker D8 Advance X-ray diffraction using Cu-Kα radiation (40 kV, 40 mA), while the XPS spectra of the catalysts were characterized by X-ray photoelectron spectroscopy/ESCA (ESCALAB 250, Thermo Fisher Scientific Company) in the Instrumental Analysis & Research Center of Sun Yat-Sen University (Guangzhou). A monochromatic Al Ka X-ray source (1486.6 eV) was used at 15 kV and 150 W, along with the pressure in the analysis chamber of about 2×10^{-7} Pa. Binding energies were referred to the C 1s peak from the carbon surface deposit at 284.8 eV.

2.5. Electrochemical measurements

The electrochemical experiments were performed on a CHI660D electrochemical workstation (Shanghai Chenhua Instrument Company) with a three-electrode system composed of the modified glass carbon electrode (GCE, 2 mm diameter) as the working electrode, saturated Ag/AgCl electrode as reference electrode (SSCE) and Pt electrode as counter electrode. For convenience, all potentials in this work were referenced to the reversible hydrogen electrode (RHE, RHE = SSCE + 0.199 + 0.0591 × pH). The catalyst-modified GCE was prepared as follows: (1) a mixture containing 5.0 mg of electrocatalyst and 1 mL of distilled water–ethanol solution (1:1, v/v ratio) was ultrasonically dispersed for 10 min; (2) 3 μL of the suspension was deposited onto a cleaned GC and dried at room temperature; (3) 5 μL of 0.5% Nafion solution was dropped on the surface as a binder to firmly affix the electrocatalysts and then dried under the air.

Before electrochemical experiments, the solution was purged with nitrogen for 10 min to remove any dissolved oxygen. Electrochemically active surface area (ECSA) of Pt nanoparticles was calculated from hydrogen electrosorption curve, which was recorded between 0.03 and 1.23 V in 0.5 M H$_2$SO$_4$ solution at a scan rate of 50 mV s^{-1}. Methanol oxidation experiments were characterized by cyclic voltammetry (CV) and chronoamperometry (CA) at room temperature. In 0.1 M H$_2$SO$_4$ + 2 M methanol, CVs were performed between 0.17 and 1.27 V at a scan rate of 50 mV s^{-1}, while CA was conducted at 0.966 V for 3000 s, and electrochemical impedance spectra (EIS) were obtained at frequencies between 100 KHz and 0.01 Hz with 12 points per decade at constant potential of 0.766 V. The CO stripping voltammetry was performed as follows. The 0.5 M H$_2$SO$_4$ solution was purged with N$_2$ for 10 min. Then, the catalysts were held at 0.03 V in CO-saturated solution for 15 min to form a saturated CO monolayer. After the excess CO dissolved in solution was further purged out with N$_2$ for 15 min, two complete oxidation/reduction cycles were recorded for in the range from 0.03 to 1.23 V at a scan rate of 10 mV s^{-1}.

3. Results and discussion

3.1. Characterization of the catalysts

In Fig. 1a, Fe$_3$O$_4$ nanoparticles were well-distributed with the average particle size of 80 nm. In Fig. 1b, Fe$_3$O$_4$@PDA nanoparticles with a typical core/shell structure were discovered, in which Fe$_3$O$_4$ nanoparticles were well wrapped in a PDA shell with the average thickness of about 7.5 nm. Furthermore, a clear interface between the Fe$_3$O$_4$ core and PDA shell indicated a tight encapsulation. In

Fig. 1c, the Fe$_3$O$_4$@PDA particles were well spread on the graphene sheets with crinkled textures, suggesting that graphene sheets can envelop the nanoparticles in a carpet-like manner without any agglomeration, which obviously enhanced the surface area and provided abundant reactive sites for anchoring much more metal nanoparticles [23]. As shown in Fig. 1d, e and f, Pt nanoparticles were uniformly distributed on the Fe$_3$O$_4$@PDA/RGO surface, and the mean Pt nanoparticles sizes were 2.11, 1.83 and 2.00 nm, respectively. As well, Fe$_3$O$_4$ was dissolved and the thicknesses of the PDA shells were clearly exposed. If more H$_2$PtCl$_6$ was added, the distance between the core and the shell of Fe$_3$O$_4$@PDA/RGO became larger, indicating that Pt deposition and Fe$_3$O$_4$ dissolution were interrelated. Furthermore, the inset of Fe$_3$O$_4$@PDA/RGO/Pt (15%) (Fig. 1f) showed that Pt nanoparticles were deposited not only on the PDA shells by the association of amino groups of the PDA surface, but also around the Fe$_3$O$_4$ core. Additionally, free Pt nano-particles can be hardly found, since the catalysts can be totally separated with a magnet.

To further analyze the as-prepared catalysts, the FT-IR spectroscopy was shown in Fig. 2. The strong band at 579 cm^{-1} was characteristic of the Fe–O vibration, while the peaks around 1622, 1420 and 878 cm^{-1} in Fig. 2B matched well with that from free 1,6-hexadiamine, which testified the successful modification of Fe$_3$O$_4$ nanoparticles surface by amino groups [22]. The peaks at 1615, 1511 and 1295 cm^{-1} were designated as the aromatic rings, the amino N–H deformation vibration and the phenolic C–OH stretching vibration, respectively (Fig. 2C), suggesting the wrapping of Fe$_3$O$_4$ by PDA. Compared with GO (Fig. 2A), the characteristic peaks of O–H stretching vibration at 3399 cm^{-1}, C=O stretching vibration at 1726 cm^{-1}, and epoxy vibration at 1221 cm^{-1} disappeared in the Fe$_3$O$_4$@PDA/RGO spectrum (Fig. 2D) [23]. After the deposition of Pt nanoparticles on the Fe$_3$O$_4$@PDA/RGO surface, the corresponding peak decreased (Fig. 2E) and the Fe–O vibration was still discovered, indicating the existence of Fe$_3$O$_4$ nanoparticles in the Fe$_3$O$_4$@PDA/RGO/Pt nanocomposite.

The structures of the as-prepared catalysts were further examined by XRD (Fig. 3). The sharp characteristic (002) diffraction peak of GO (Fig. 3A) at $2\theta \approx 11.1°$ (corresponding to the interlayer spacing of 0.40 nm) combined with the near elimination of the diffraction peak at $2\theta \approx 42.4°$ (100) of the hexagonal structure of graphite confirmed the successful oxidation of the graphite [24]. In Fig. 3B, the six characteristic diffraction peaks at $2\theta \approx 30.1°$, 35.4°, 43.1°, 53.6°, 57.2° and 62.9° were corresponded to the (220), (311), (400), (422), (511) and (440) planes of Fe$_3$O$_4$, respectively [22]. In Fig. 3C, the XRD pattern of Fe$_3$O$_4$@PDA was similar to that of the original Fe$_3$O$_4$ nanoparticles even Fe$_3$O$_4$ was wrapped in a PDA shell. For Fe$_3$O$_4$@PDA/RGO (Fig. 3D), the sharp diffraction peak in GO dramatically decreased, thus GO was reduced [23]. Fig. 3E, F and G showed the XRD patterns of Fe$_3$O$_4$@PDA@RGO@Pt catalysts with different Pt contents, where the diffraction peaks at 39.8°, 46.7° and 67.4° can be assigned to Pt(111), Pt(200) and Pt(220), respectively [25], indicating the existence of Pt nanoparticles. Moreover, as the Pt content increased, the intensity of Pt peaks increased and Fe$_3$O$_4$ peaks decreased, respectively.

XPS has been often used to get the information of elements in different chemical neighborhoods on the surface. As shown in Fig. 4a, C, O, N, Pt, Fe can be found in the XPS survey spectrum of the Fe$_3$O$_4$@PDA/RGO/Pt. For the high resolution of C 1s spectrum of Fe$_3$O$_4$@PDA/RGO (Fig. 4b), the peak at 284.6 eV can be assigned to the sp^2 C–C bond, while the peaks at 285.8 eV and 287.7 eV, 289.9 eV were corresponded to C–OH, C=O and O=C–O configurations, respectively [26]. After reduction, oxygen-containing carbon of GO reduced significantly, indicating an efficient reduction through reaction with PDA by a mild hydrothermal process. In Fig. 4c, the Fe 2p spectrum were deconvolved into two pairs of
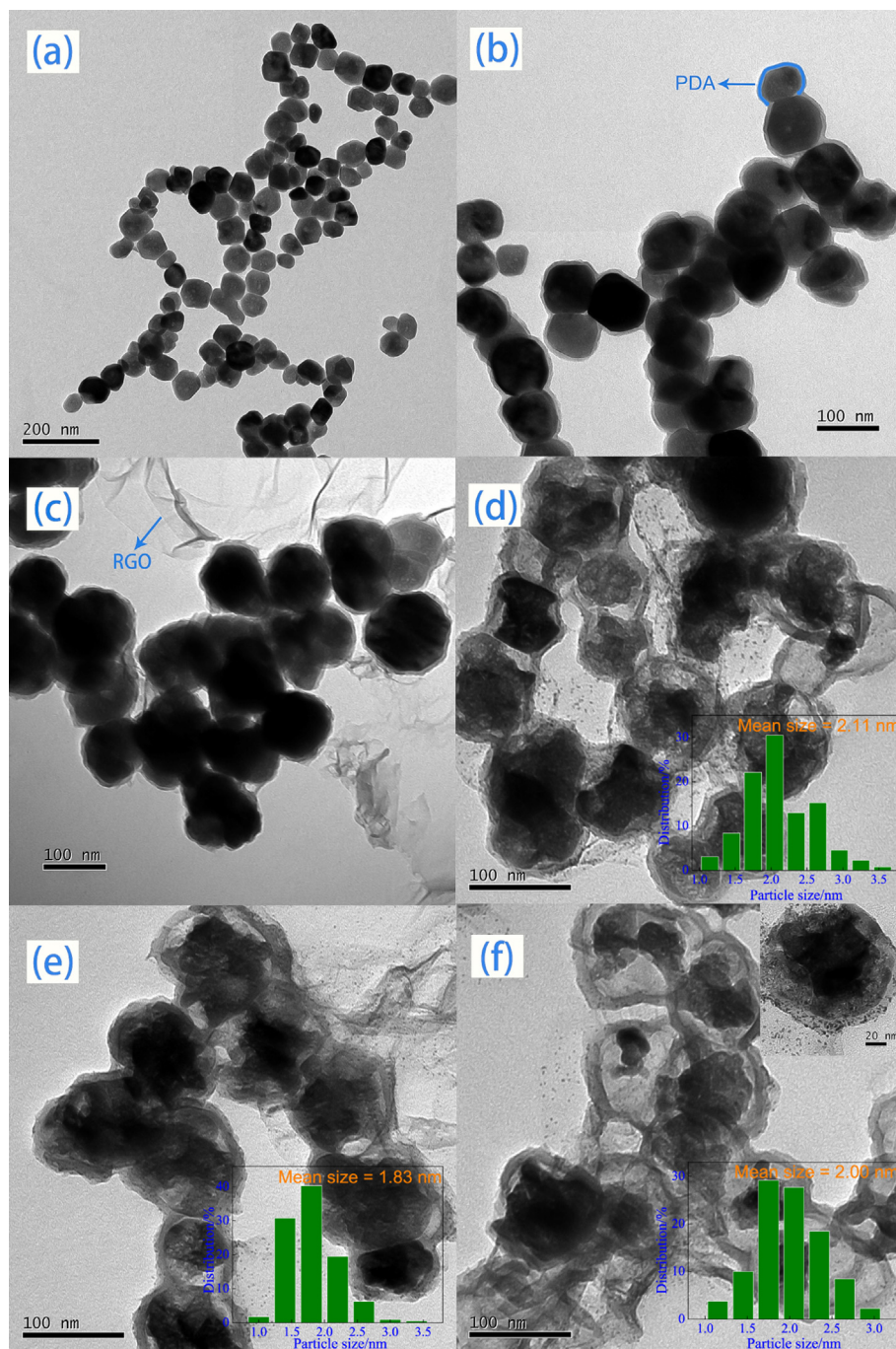
Fig. 1. TEM images of (a) Fe_3O_4, (b) Fe_3O_4@PDA, (c) Fe_3O_4@PDA/RGO, (d) Fe_3O_4@PDA/RGO/Pt (9%), (e) Fe_3O_4@PDA/RGO/Pt (12%) and (f) Fe_3O_4@PDA/RGO/Pt (15%).

doublets which were corresponded to Fe $2p_{1/2}$ and Fe $2p_{3/2}$ of Fe (III) and Fe (II) chemical states. The stronger doublet peaks at 713.1 eV and 726.6 eV could be attributed to Fe (III) ionic, while the weaker doublet peaks at 711.2 eV and 724.7 eV were assigned to Fe (II) ionic [27]. The binding energies of the Fe 2p peak and the relative intensities of Fe species for different catalysts were shown in Table 1. Compared with Fe_3O_4@PDA/RGO, the peaks of Fe (III) and Fe (II) for Fe_3O_4@PDA/RGO/Pt were both shifted by 0.8 eV, reflecting the interaction between Pt and Fe_3O_4 [28]. The relative intensity of Fe (III) chemical state for the Fe_3O_4@PDA/RGO/Pt was higher than that for the Fe_3O_4@PDA/RGO, while the relative intensity of Fe (II) chemical state was correspondingly lower, suggesting that some Fe (II) ionic species in Fe_3O_4 were oxidized to Fe (III) ionic species.

Furthermore, as shown in Fig. 4d, the Pt 4f spectrum of Fe_3O_4@PDA/RGO/Pt were deconvolved into two components which had a spin-orbit splitting of $4f_{7/2}$ and $4f_{5/2}$ states of ca. 3.35 eV and relative peak area close to the expected ratio of 4:3. The peaks at 74.85 ($4f_{5/2}$) and 71.50 eV ($4f_{7/2}$) were attributed to Pt (0), while the peaks at 75.83 ($4f_{5/2}$) and 72.48 eV ($4f_{7/2}$) were ascribed to Pt (II) from PtO or $Pt(OH)_2$ [11]. The peak of Pt (0) shifted toward higher binding energy slightly with respect to the literature value of 71.2 eV, indicating an interaction between Pt particles and Fe_3O_4@PDA/RGO support [29]. In addition, the amounts of Pt species were calculated from the relative intensities of these two components, and the results were shown in Table 2. The relative intensity of Pt (II) chemical state for
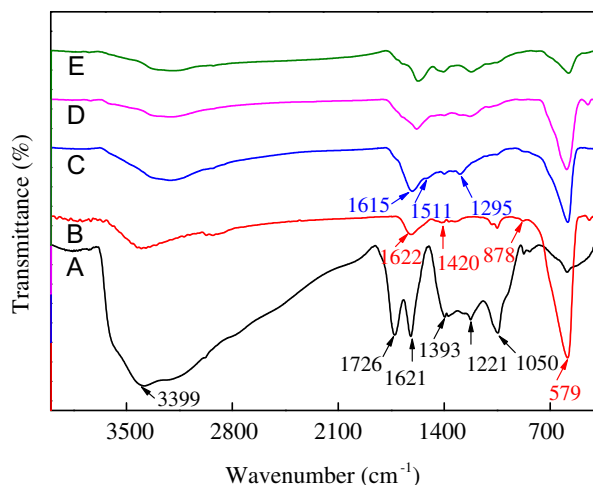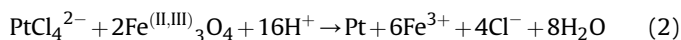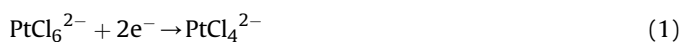
Fig. 2. FT-IR spectra of (A) GO, (B) Fe_3O_4, (C) Fe_3O_4@PDA, (D) Fe_3O_4@PDA/RGO and (E) Fe_3O_4@PDA/RGO/Pt.

Fe_3O_4@PDA/RGO/Pt was higher than that for Pt/graphene. Based on the fact that the standard electrode potential of $Pt(OH)_2$/Pt redox pair (0.14 V vs. SHE) was lower than that of the Fe^{3+}/Fe^{2+} redox pair (0.77 V vs. SHE), metallic Pt can be oxidized to $Pt(OH)_2$ or other Pt-containing oxides in the presence of Fe (III) ionic, while the resultant Fe (II) could be easily oxidized to Fe (III) again by air [30]. Therefore, XPS results showed that Pt (II) of Pt/ Fe_3O_4@PDA/RGO was higher than that of Pt/graphene, accompanied by a higher relative content of Fe (III) in Pt/Fe_3O_4@PDA/ RGO than that of Fe_3O_4@PDA/RGO.

3.2. The plausible reaction mechanism

The plausible overall Pt deposition process can be suggested as following [31]:

$$PtCl_6^{2-} + 2e^- \rightarrow PtCl_4^{2-} \tag{1}$$

$$PtCl_4^{2-} + 2Fe^{(II,III)}_3O_4 + 16H^+ \rightarrow Pt + 6Fe^{3+} + 4Cl^- + 8H_2O \tag{2}$$

By ethylene glycol at high temperature, most of $PtCl_4^{2-}$ ions were reduced to Pt nanoparticles and deposited on Fe_3O_4@PDA/RGO, while the galvanic reaction of $PtCl_6^{2-}$ to $PtCl_4^{2-}$ can still occur [30]. With the aid of $PtCl_4^{2-}$, some Fe_3O_4 in Fe_3O_4@PDA/RGO were oxidized and dissolved into the soluble ionic species, thus the yolk–shell nanocomposite was formed. The experimental phenomena further confirmed this supposition. As shown in Fig. S1 (Supporting Information), the color of the separation solution of Fe_3O_4@PDA/ RGO/Pt catalyst was light yellow, while it was colorless for Fe_3O_4@PDA/RGO. Therefore, it can be concluded that Fe_3O_4 was dissolved to a certain degree during the Pt deposition to form the york–shell composite.

Furthermore, the high separation efficiency of Fe_3O_4 in this nanocomposite was monitored (Fig. S1). After centrifugation at 3000 rpm or 6000 rpm for 5 min, the separation solution of Pt/ graphene still showed a few black Pt nanoparticles. Only after centrifugation at 9000 rpm for 5 min, no free Pt nanoparticles existed. Due to the amino groups of Fe_3O_4@PDA, Pt nanoparticles can be deposited around them without freely dispersing in the solution, and also be easily washed in a few seconds. Moreover, the original hydrothermal-treated graphene solution was still a homogeneous black suspension even after its centrifugation at 12,000 rpm for 8 min, while the solution was clean and
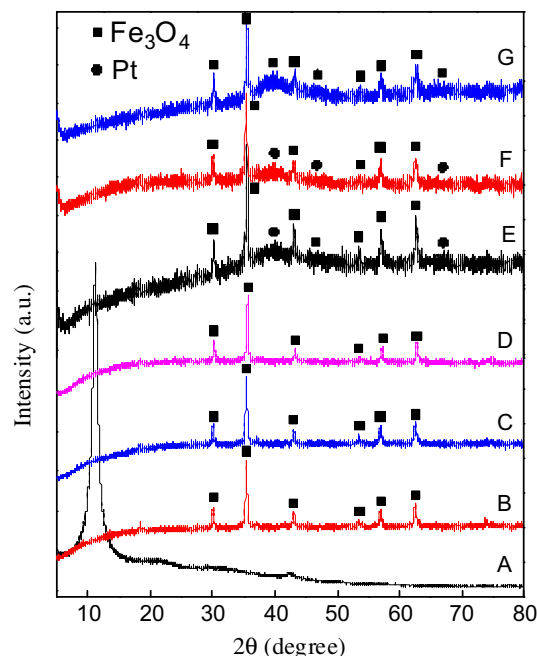

Fig. 3. XRD patterns of (A) GO, (B) Fe_3O_4, (C) Fe_3O_4@PDA, (D) Fe_3O_4@PDA/RGO, (E) Fe_3O_4@PDA/RGO/Pt (9%), (F) Fe_3O_4@PDA/RGO/Pt (12%) and (G) Fe_3O_4@PDA/RGO/Pt (15%).

Table 1
XPS analysis: binding energies and relative intensities of different Fe species in Fe_3O_4@PDA/RGO/Pt and Fe_3O_4@PDA/RGO.

Samples	Fe (III) $2p_{1/2}$	Fe (II) $2p_{1/2}$	Fe (III) $2p_{3/2}$	Fe (II) $2p_{3/2}$	Fe (III) (%)	Fe (II) (%)
Fe_3O_4@PDA/RGO/Pt	726.6	724.7	713.1	711.2	55.76	44.24
Fe_3O_4@PDA/RGO	725.8	723.9	712.3	710.4	50.57	49.43

transparent in the presence of Fe_3O_4@PDA with a magnet, further proving the separation ability of Fe_3O_4 in this nanocomposite.

3.3. Electrocatalytic activity for methanol oxidation reaction

CV is a convenient and efficient tool to estimate the ECSA on an electrode. The ECSA not only provides important information regarding the number of available electrochemically active sites, but also is essential for comparing different electrocatalytic supports. The tests were measured in N_2-saturated 0.5 M H_2SO_4 solution at a scan rate of 50 mV s^{-1}, as shown in Fig. 5a. In the potential range of 0.05 V–0.40 V, typical hydrogen adsorption and desorption peaks from Pt were observed using the composite as the supporting materials. The integrated area under the adsorption peak represented the total charge hydrogen adsorption (Q_H), and was used to determine ECSA by the following equation [32,33]:

Table 2
XPS analysis: binding energies and relative intensities of different Pt species in Fe_3O_4@PDA/RGO/Pt and Pt/graphene.

Samples	Pt (II) $4f_{5/2}$	Pt (0) $4f_{5/2}$	Pt (II) $4f_{7/2}$	Pt (0) $4f_{7/2}$	Pt (II) (%)	Pt (0) (%)
Fe_3O_4@PDA/RGO/Pt	75.83	74.85	72.48	71.50	48.92	51.08
Pt/graphene	76.01	74.86	72.66	71.51	36.56	63.44

$$\text{ECSA}\left[\text{cm}^2\,\text{g}^{-1}\text{of Pt}\right] = \frac{\text{charge}\left[Q_H, \mu\text{C cm}^{-2}\right]}{210\left[\mu\text{C cm}^{-2}\right] \times \text{electrode loading}\left[\text{g of Pt cm}^{-2}\right]} \tag{3}$$

Therefore, Fe_3O_4@PDA/RGO/Pt with 12%, 15% and 9% of Pt loading showed the ECSA value of 49.2, 42.8 and 33.3 m^2 g^{-1}, whereas the Pt/graphene catalyst showed ECSA value of 25.2 m^2 g^{-1}. Therefore, ECSA of Fe_3O_4@PDA/RGO/Pt (12%) was about 1.95 times that of Pt/graphene. The reason may be as following: (1) The smaller size and much better dispersion of Pt nanoparticles on the Fe_3O_4@PDA/RGO as displayed in the TEM image than Pt/graphene in earlier work [34,35]; (2) The synergetic cocatalytic effect at the heterojunction interfaces formed between the Pt nanocrystal and the Fe_3O_4@PDA/RGO support [36]; (3) The presence of large amount of functional groups ($-NH_2$) on the surface of the PDA, which enabled many Pt nanoparticles to be tightly immobilized on the support surface [37]. Due to the relative higher ECSA value, such Fe_3O_4@PDA/RGO/Pt catalyst can afford more active sites for electrochemical reaction, therefore providing the potential for better catalytic activity towards DMFC.

The electrocatalytic activities of the as-prepared catalysts to methanol oxidation were characterized by CV in N_2-saturated 0.1 M H_2SO_4 + 2 M CH_3OH solution at a scan rate of 50 mV s^{-1}. As shown in Fig. 5b, all curves showed two typical oxidation peaks, in which a methanol oxidation peak during the forward scan at around 0.87–1.07 V, while the reverse oxidation peak in the backward scan at around 0.67–0.87 V might be attributed to the removal of the incomplete oxidized carbonaceous species during the forward scan, such as CO, $HCOO^-$ and HCO^- [1,11]. Especially, the methanol oxidation current density peak during the forward scan can indicate the electrocatalytic activity for methanol oxidation. The forward peak current density of Fe_3O_4@PDA/RGO/Pt (12%), Fe_3O_4@PDA/RGO/Pt (15%) and Fe_3O_4@PDA/RGO/Pt (9%) reached

385.3, 316.3 and 200.3 mA mg$_{Pt}^{-1}$, almost 2.6, 2.2 and 1.4 times as high as that of Pt/graphene (146.1 mA mg$_{Pt}^{-1}$), indicating the Fe_3O_4@PDA/RGO/Pt (12%) catalyst exhibited the highest peak current density. There were two major factors for the Fe_3O_4@PDA/Pt nanocomposite with higher activity in electrochemical performance: (1) the presence of large amount of functional group ($-NH_2$) on the surface of the PDA, which can chelate with more Pt^{4+} and enhance the loading of Pt nanoparticles; (2) better dispersion of Pt nanoparticles on the Fe_3O_4@PDA/RGO surface with high surface area and high conductivity should be also emphasized [38].

In addition, the ratio of the forward oxidation current peak (I_f) to the reverse current peak (I_b), I_f/I_b, is an important index of the catalyst tolerance to the poisoning species on the surface of the electrode [1,38]. The low I_f/I_b value usually indicates poor oxidation of methanol to CO_2 and excessive accumulation of residual carbon species on catalyst surface, while a higher I_f/I_b value shows the reverse case. The I_f/I_b values of Fe_3O_4@PDA/RGO/Pt with 9%, 12% and 15% of Pt loading were 1.97, 1.63 and 1.40, respectively, which were substantially higher than that of the Pt/graphene (1.35). Therefore, more intermediate carbonaceous species were oxidized to carbon dioxide on the Fe_3O_4@PDA/RGO/Pt catalysts, suggesting Fe_3O_4 played an important role in the catalyst tolerance to the poisoning species. Except that Fe_3O_4 can produce OH_{ads} species at lower potential to oxidize CO, it can also make the Pt–CO bond weaker and thereby improve the electrocatalytic activity of the catalyst towards methanol oxidation [1,6].

Furthermore, to compare the stability of the catalysts toward methanol oxidation, chronoamperometry tests were investigated in N_2-saturated 0.1 M H_2SO_4 + 2 M CH_3OH solution for 3000 s at

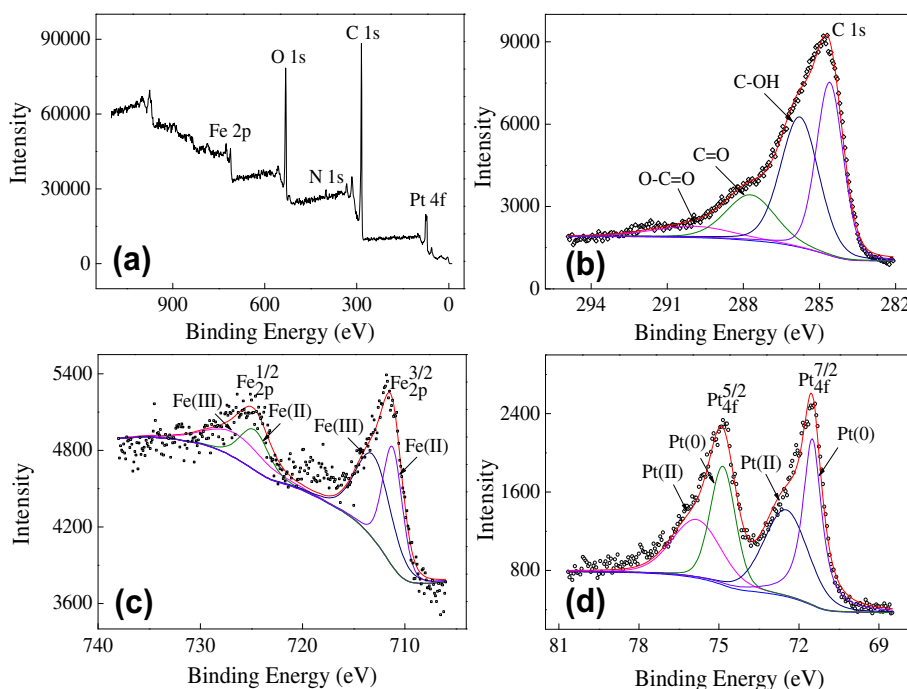**Fig. 4.** XPS survey spectra of (a) Fe_3O_4@PDA/RGO/Pt, (b) C 1s for Fe_3O_4@PDA/RGO, (c) Fe 2p and (d) Pt 4f for Fe_3O_4@PDA/RGO/Pt.
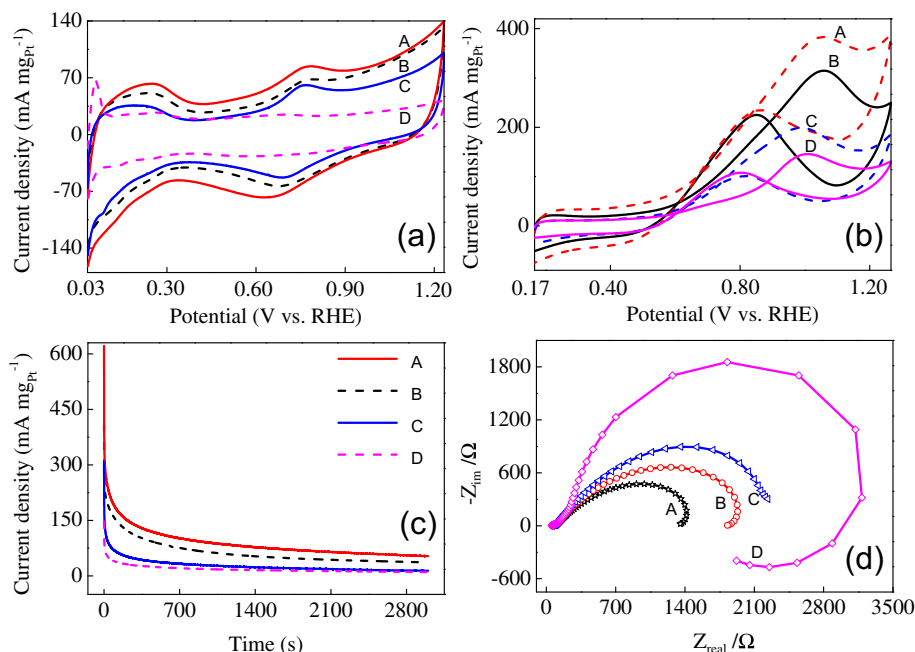
Fig. 5. CV curves (a, b) of (A) Fe₃O₄@PDA/RGO/Pt (12%), (B) Fe₃O₄@PDA/RGO/Pt (15%), (C) Fe₃O₄@PDA/RGO/Pt (9%), and (D) Pt/graphene in N₂-saturated (a) 0.5 M H₂SO₄, (b) 0.1 M H₂SO₄ + 2 M CH₃OH at a scan rate of 50 mV s⁻¹. Chronoamperometric (c) and EIS (d) of (A) Fe₃O₄@PDA/RGO/Pt (12%), (B) Fe₃O₄@PDA/RGO/Pt (15%), (C) Fe₃O₄@PDA/RGO/Pt (9%), and (D) Pt/graphene for methanol oxidation in N₂-saturated 0.1 M H₂SO₄ + 2 M CH₃OH at a constant potential of (c) 0.966 V and (d) 0.766 V.

room temperature and a constant potential of 0.966 V. As shown in Fig. 5c, it can be found that the current decreased rapidly at the beginning, which was due to the catalyst poison by the accumulation of intermediate CO-like species on Pt active sites. After the long-time operation, the currents of methanol oxidation on all catalysts arrived at a stable stage, which suggested that the processes of accumulation and removal of CO-like species reached a balance [2]. The Fe₃O₄@PDA/RGO/Pt (12%) catalyst exhibited the highest current density with the lowest decay rate as compared to other catalysts, indicating Fe₃O₄@PDA/RGO can improve the electrocatalytic activity and stability of the catalysts as well as CO poisoning tolerance of the Pt nanoparticles significantly [5].

EIS was another effective technique to obtain the charge transfer resistance. The smaller of the diameter of Nyquist plot, the better of the catalytic activity [5]. It was well known that the smaller charge transfer resistance was attributed to the formation of chemisorbed hydroxyl species, which facilitated the oxidation of CO_{ads} originated from methanol oxidation [2]. Fig. 5d showed Nyquist plots in N₂-saturated 0.1 M H₂SO₄ + 2 M CH₃OH solution at a constant potential of 0.766 V, where the diameter for Fe₃O₄@PDA/RGO/Pt yolk/shell catalysts were smaller than that of Pt/graphene, further demonstrating that the yolk/shell structure possessed lower resistance and thus allowed a faster electron transfer [39]. In addition, The Fe₃O₄@PDA/RGO/Pt (12%) exhibited the smallest diameter of Nyquist plot, indicating a smaller reaction resistance and higher conductivity that can provide higher electrocatalytic activity for methanol oxidation than other catalysts.

As CO_{ads} species were the main poisoning intermediate during the methanol oxidation, a perfect catalyst should possess excellent CO oxidation and anti-poisoning ability, thus it can oxidize more CO or oxidize CO more quickly at a lower potential [6,11]. The CO stripping voltammograms were shown in Fig. 6. In all curves, the CO oxidation peaks were about 0.850 V, whereas no CO oxidation was monitored in the second scan, indicating that the CO_{ads} species were completely oxidized during the first forward scan. The peak potentials for CO oxidation on Fe₃O₄@PDA/RGO/Pt

with Pt loading of 9%, 12% and 15% were 0.855 V, 0.853 V and 0.860 V, respectively, all of which were smaller than that on Pt/graphene (0.870 V). Further, the onset potential of CO oxidation can be used to characterize the easiness of CO oxidation [6,40]. Among all catalysts, 12% of Pt loading presented the lowest onset potential of CO oxidation (0.616 V), which was 166 mV lower than that on the Pt/graphene catalyst (0.782 V). Therefore, the adsorbed CO can be oxidized more quickly and readily on Fe₃O₄@PDA/RGO/Pt catalyst than Pt/graphene catalyst, which were attributed to the fact that Fe₃O₄ can supply an oxygen containing surface to remove strongly absorbed CO by favoring the bi-functional mechanism [3,41]:
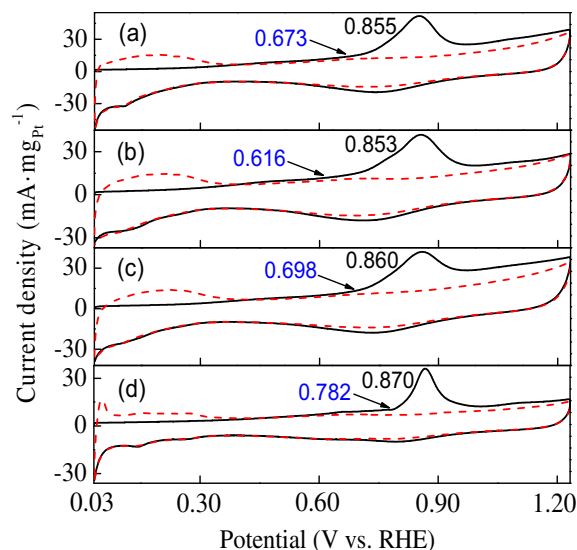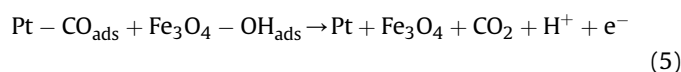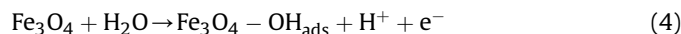

Fig. 6. CO-stripping voltammograms of (a) Fe₃O₄@PDA/RGO/Pt (9%), (b) Fe₃O₄@PDA/RGO/Pt (12%), (c) Fe₃O₄@PDA/RGO/Pt (15%) and (d) Pt/graphene.

$$Fe_3O_4 + H_2O \rightarrow Fe_3O_4 - OH_{ads} + H^+ + e^- \quad (4)$$

$$Pt - CO_{ads} + Fe_3O_4 - OH_{ads} \rightarrow Pt + Fe_3O_4 + CO_2 + H^+ + e^- \quad (5)$$

OH_{ads} can be easily generated on Fe_3O_4, which can easily oxidize CO-like species on Pt sites, thus Fe_3O_4@PDA/RGO/Pt catalysts showed perfect application in DMFC.

4. Conclusion

In summary, a novel Fe_3O_4@PDA/RGO/Pt yolk/shell nanocomposite was fabricated by using PDA as a moderate modifier as well as a coupling agent for the assembly of modified graphene oxide and Pt nanoparticles on Fe_3O_4 cores, which was characterized by TEM, XPS, XRD and FT-IR. Its electrochemical oxidation of methanol was investigated using cyclic voltammetry, chronoamperometry, electrochemical impedance spectra and CO-stripping voltammetry. Results showed that the Fe_3O_4@PDA/RGO/Pt catalyst exhibited lower overpential, higher electrocatalytic activity and notably stability for methanol oxidation than Pt/graphene. Thus, this work supplied a unique Fe_3O_4@PDA/RGO/Pt nanocomposite as an efficient way to prepare other york/shell nanostructure, which will improve their performance in many fields including electrocatalysis, photocatalysis and biosensor.

Acknowledgments

Appendix A. Supplementary data

Supplementary data related to this article can be found at http://dx.doi.org/10.1016/j.jpowsour.2013.08.055.

References

[1] Y.J. Liu, Y.Q. Huang, Y. Xie, Z.H. Yang, H.L. Huang, Q.Y. Zhou, Chem. Eng. J. 197 (2012) 80–87.
[2] X. Jin, B. He, J. Miao, J. Yuan, Q. Zhang, L. Niu, Carbon 50 (2012) 3083–3091.
[3] J.M. Léger, S. Rousseau, C. Coutanceau, F. Hahn, C. Lamy, Electrochim. Acta 50 (2005) 5118–5125.
[4] C. Lu, C. Rice, R.I. Masel, P.K. Babu, P. Waszczuk, H.S. Kim, E. Oldfield, A. Wieckowski, J. Phys. Chem. B 106 (2002) 9581–9589.
[5] D. Gu, Y. Chu, Z. Wang, Z. Jiang, G. Yin, Y. Liu, Appl. Catal. B Environ. 102 (2011) 9–18.
[6] H. Song, X. Qiu, F. Li, Appl. Catal. A Gen. 364 (2009) 1–7.
[7] J. Li, J. Ren, G. Yang, P. Wang, H. Li, X. Sun, L. Chen, J. Ma, R. Li, Mater. Sci. Eng. B 172 (2010) 207–212.
[8] A. Lu, E.L. Salabas, F. Schüth, Angew. Chem. Int. Ed. 46 (2007) 1222–1244.
[9] C. Feng, T. Takeuchi, M.A. Abdelkareem, T. Tsujiguchi, N. Nakagawa, J. Power Sources 242 (2013) 57–64.
[10] N.D. Luong, Y. Lee, J. Nam, J. Mater. Chem. 18 (2008) 4254–4259.
[11] Y. Huang, H. Huang, Y. Liu, Y. Xie, Z. Liang, C. Liu, J. Power Sources 201 (2012) 81–87.
[12] H. Wang, J.T. Robinson, X. Li, H. Dai, J. Am. Chem. Soc. 131 (2009) 9910–9911.
[13] S.D. Perera, R.G. Mariano, N. Nijem, Y. Chabal, J.P. Ferraris, K.J. Balkus Jr., J. Power Sources 215 (2012) 1–10.
[14] L.Q. Xu, W.J. Yang, K. Neoh, E. Kang, G.D. Fu, Macromolecules 43 (2010) 8336–8339.
[15] L. Yang, W.A. Yee, S.L. Phua, J. Kong, H. Ding, J.W. Cheah, X. Lu, RSC Adv. 2 (2012) 2208–2210.
[16] X. Wang, X. Li, L. Zhang, Y. Yoon, P.K. Weber, H. Wang, J. Guo, H. Dai, Science 324 (2009) 768–771.
[17] D. Wei, Y. Liu, Y. Wang, H. Zhang, L. Huang, G. Yu, Nano Lett. 9 (2009) 1752–1758.
[18] P. Chen, J. Yang, S. Li, Z. Wang, T. Xiao, Y. Qian, S. Yu, Nano Energy 2 (2013) 249–256.
[19] H. Liu, J. Qu, Y. Chen, J. Li, F. Ye, J.Y. Lee, J. Yang, J. Am. Chem. Soc. 134 (2012) 11602–11610.
[20] L. Kuai, S. Wang, B. Geng, Chem. Commun. 47 (2011) 6093–6095.
[21] J. Liu, H.Q. Yang, F. Kleitz, Z.G. Chen, T. Yang, E. Strounina, G.Q.M. Lu, S.Z. Qiao, Adv. Funct. Mater. 22 (2012) 591–599.
[22] L. Wang, J. Bao, L. Wang, F. Zhang, Y. Li, Chem. Eur. J. 12 (2006) 6341–6347.
[23] T. Zeng, X. Zhang, Y. Ma, H. Niu, Y. Cai, J. Mater. Chem. 22 (2012) 18658–18663.
[24] D.C. Marcano, D.V. Kosynkin, J.M. Berlin, A. Sinitskii, Z. Sun, A. Slesarev, L.B. Alemany, W. Lu, J.M. Tour, ACS Nano 4 (2010) 4806–4814.
[25] J. Qi, L. Jiang, Q. Tang, S. Zhu, S. Wang, B. Yi, G. Sun, Carbon 50 (2012) 2824–2831.
[26] H. Cong, X. Ren, P. Wang, S. Yu, ACS Nano 6 (2012) 2693–2703.
[27] T. Fujii, F. De Groot, G.A. Sawatzky, F.C. Voogt, T. Hibma, K. Okada, Phys. Rev. B 59 (1999) 3195–3202.
[28] D. Andreeva, T. Tabakova, V. Idakiev, P. Christov, R. Giovanoli, Appl. Catal. A Gen 169 (1998) 9–14.
[29] D.R.M. Godoi, J. Perez, H.M. Villullas, J. Power Sources 195 (2010) 3394–3401.
[30] J. Zou, A.D. Martin, B. Zdyrko, I. Luzinov, C.L. Raston, K.S. Iyer, Chem. Commun. 47 (2011) 5193–5195.
[31] Y. Sun, B. Mayers, Y. Xia, Adv. Mater. 15 (2003) 641–646.
[32] B. Wu, D. Hu, Y. Kuang, B. Liu, X. Zhang, J. Chen, Angew. Chem. Int. Ed. 48 (2009) 4751–4754.
[33] S. Sun, G. Zhang, D. Geng, Y. Chen, R. Li, M. Cai, X. Sun, Angew. Chem. Int. Ed. 123 (2011) 442–446.
[34] Y. Li, W. Gao, L. Ci, C. Wang, P.M. Ajayan, Carbon 48 (2010) 1124–1130.
[35] L.S. Zhang, X.Q. Liang, W.G. Song, Z.Y. Wu, Phys. Chem. Chem. Phys. 12 (2010) 12055–12059.
[36] K.W. Kim, S.M. Kim, S. Choi, J. Kim, I.S. Lee, ACS Nano 6 (2012) 5122–5129.
[37] J. Si, H. Yang, Mater. Chem. Phys. 128 (2011) 519–524.
[38] S. Guo, S. Dong, E. Wang, ACS Nano 4 (2010) 547–555.
[39] M. Shao, F. Ning, J. Zhao, M. Wei, D.G. Evans, X. Duan, Adv. Funct. Mater. 23 (2013) 3513–3518.
[40] H. Song, P. Xiao, X. Qiu, W. Zhu, J. Power Sources 195 (2010) 1610–1614.
[41] F. Han, X. Wang, J. Lian, Y. Wang, Carbon 50 (2012) 5498–5504.